

This is the pre-peer reviewed version of the article “Cellular uptake of mildly oxidized nanographene for drug-delivery applications” which has been published in the final form in [ACS Applied Nano Materials \(ACS\)](#), DOI: [10.1021/acsanm.9b02035](#). This article may be used for non-commercial purposes.

Cellular Uptake of Mildly Oxidized Nano-Graphene for Drug-Delivery Applications

M. Mugnano^{*,†}, G. C. Lama^{*,‡}, R. Castaldo[‡], V. Marchesano[†], F. Merola[†], D. del Giudice[†], A. Calabuig[†], G. Gentile[‡], V. Ambrogio[§], P. Cerruti[‡], P. Memmolo[†], V. Pagliarulo[†], P. Ferraro[†], S. Grilli[†]

[†]*Institute of Applied Science & Intelligent Systems ‘E. Caianiello’, National Council of Research (CNR-ISASI), Via Campi Flegrei 34, 80078 Pozzuoli (NA), Italy*

[‡]*Institute for Polymers, Composites and Biomaterials, National Council of Research (CNR-IPCB), Via Campi Flegrei, 34, 80078 Pozzuoli (NA), Italy*

[§]*Department of Chemical, Materials and Industrial Production Engineering, University of Naples “Federico II”, Piazzale Tecchio 80, 80125 Napoli, Italy*

ABSTRACT: Graphene family materials (GFM) have large perspectives for drug delivery applications but their internalization in live cells is under investigation in a wide variety of studies in order to assess the best conditions for efficient cellular uptake. Here we show that mild oxidation of graphene nanoplatelets produces nano-graphene oxide (nGO) particles which are massively internalized into the cell cytoplasm. This remarkable uptake of nGO in NIH-3T3 cells has never been observed before. We performed vitality tests for demonstrating the biocompatibility of the material and analyzed the internalization mechanism under different oxidation degrees and concentrations. Moreover, we evaluated quantitatively, for the first time, the cell volume variation after nGO internalization in live cells through a label-free digital holographic imaging technique and in quasi real-time modality, thus avoiding the time consuming and detrimental procedures usually employed by electron-based microscopy. The results demonstrate that nGO formulations with a tailored balance between exposed surface and content of functional groups are very promising in drug delivery applications.

KEYWORDS: *nano-graphene oxide, nanoplatelets, graphene-based nanomaterials, cellular uptake, cytotoxicity, cell culture, digital holography*

1. Introduction

Graphene is a two-dimensional (2D) material made of carbon atoms bonded together in a repeating pattern of hexagons. Its outstanding physical properties were reported for the first time in 2004 [1]

and, since then, it attracts lots of interest for its unique properties such as high mechanical strength, specific surface area and high thermal and electrical conductivity [2] [3] [4] [5] [6].

Different techniques are continuously developed and refined in order to obtain graphene family materials (GFM) with tailored properties. For instance, strong oxidizing agents can be used to produce an oxidized form of graphene, known as graphene oxide (GO) [7]. In this case, the oxygen-based functional groups reduce the thermal stability of graphene but are of crucial importance for promoting the compatibility with polar solvents [8].

The first application of a GFM in a biological environment dates back to 2008, when Dai et al. demonstrated the ability of nanosized GO (nGO) to loading and delivering aromatic, water insoluble drugs [9]. A few years later, Wang et al. investigated for the first time the effects of GO on human fibroblast cells and mice, thus presenting the first results on the biocompatibility of GFM [10]. Many other biomedical applications of GFM have been studied, such as drug and gene delivery [11] [12], bioimaging [13], biosensors [14] [15] and tissue engineering [16]. Valuable reviews can be found in literature on the diverse applications [17] [18]. In particular, for all of those applications related to drug and gene delivery, elucidating the mechanism of cellular uptake and cytotoxicity of GFM are of crucial importance.

Most of the works published in literature on the interaction of live cells with GFM focus their attention on specific parameters. Among them, conjugation with specific compounds appears to increase GFM hydrophilicity and stability in biological media, thus favoring cellular uptake [19] [20] [21] [22] [23] [24] [25] [26]. Several researchers have studied both experimentally and theoretically the mechanisms of interaction of GFM with the lipid bilayers of the cellular membranes [27] [28] [29] [30], in order to better understand the rules that govern the cellular uptake. The biocompatibility of GFM depends also on the oxidation degree of the selected carbon-based material, however additional studies are needed to clarify the effects on different cell lines [23] [31] [32]. Another family of works focus their attention on the size-dependent effects, but poor information is available on the cell viability for the same type of GFM [33] [34] [35] [36] [37].

In this framework, general conclusions on the cellular uptake of GFM and relative cytotoxicity cannot be drawn. First of all, different graphene forms have been investigated – such as few-layer graphene, graphene nanoplatelets, graphene nanosheets, graphene nanoribbons, GO, reduced GO – which exhibit unique physicochemical properties and hence exert different toxicological effects [38] [39] [40]. Moreover, the *in vitro* studies are not fully comparable due to the different nature of the countless cellular lines investigated in each research and to the great amount of parameters varied for each GFM (e.g. concentration, shape, surface functionalization, lateral dimension, exposure time, oxidation degree) [20] [34] [41] [42].

Nevertheless, interactions between GFMs and proteins are better elucidated [43] [44]. Among them, strong π - π stacking non-covalent interactions, involving the π electrons of GFM and the aromatic residues of proteins in cell culture media, lead to the formation of protein corona complexes [44] [45]. Herein we show that mild oxidation of graphene nanoplatelets (GNP) results in high surface area nGO particles efficiently uptaken by cell. Compared to the above-mentioned works, we use here a simple oxidation technique that makes GNP biocompatible and bio-absorbable, thus avoiding iterative and harsh oxidation or conjugation procedures. We used bright and fluorescence field observation for qualitative characterization of the cellular uptake at different exposure times, and nGO concentration and oxidation degrees. Moreover, we developed a quantitative phase-contrast imaging system, based on digital holography (DH) in microscope configuration [46] [47] [48] [49] [50] [51], for the quantitative evaluation of nGO internalization. This non-invasive and label-free technique enabled to characterize the cellular uptake of nGO for the first time on live cells, without time-consuming and/or detrimental labelling procedures, and in quasi real-time modality.

Even though an efficient uptake of GFM has been reported in literature [35] [36], to the best of our knowledge, the massive cytoplasm filling achieved in this work has never been observed nor characterized in live cells, disclosing relevant opportunities for drug release applications. Recently, Castaldo et al. demonstrated how mildly oxidized nGO platelets possess significant adsorption ability toward an organic dye, methylene blue (MB), [52] which is also used as a drug for the treatment of neurodegenerative disorders, such as Alzheimer's and Parkinson's disease. [53, 54, 55] Therefore, the high efficient cellular uptake demonstrated here, combined with the preliminary results on the adsorption of aromatic dyes [52], reveal that the mild oxidation of GNP produces a very promising nanocarrier for highly efficient drug delivery. Moreover, the DH results open the route to the possibility of live monitoring of drug internalization.

2. Results and Discussion

2.1. Characterization of nGO

We studied the cellular uptake of mildly oxidized nGO under three different oxidation degrees, well below those usually reported in literature. The three different nGO materials are coded here as *nGO1*, *nGO2*, and *nGO3* where the increasing number refers to a slight growth in oxidation extent. A commercial GO (*GO-c*) was used as reference material. For all samples three different concentrations in water were used (**Table S1**). The *nGO_x* samples were prepared starting from a commercial GNP using a modified Hummers' procedure [52], as detailed in **Table S1**.

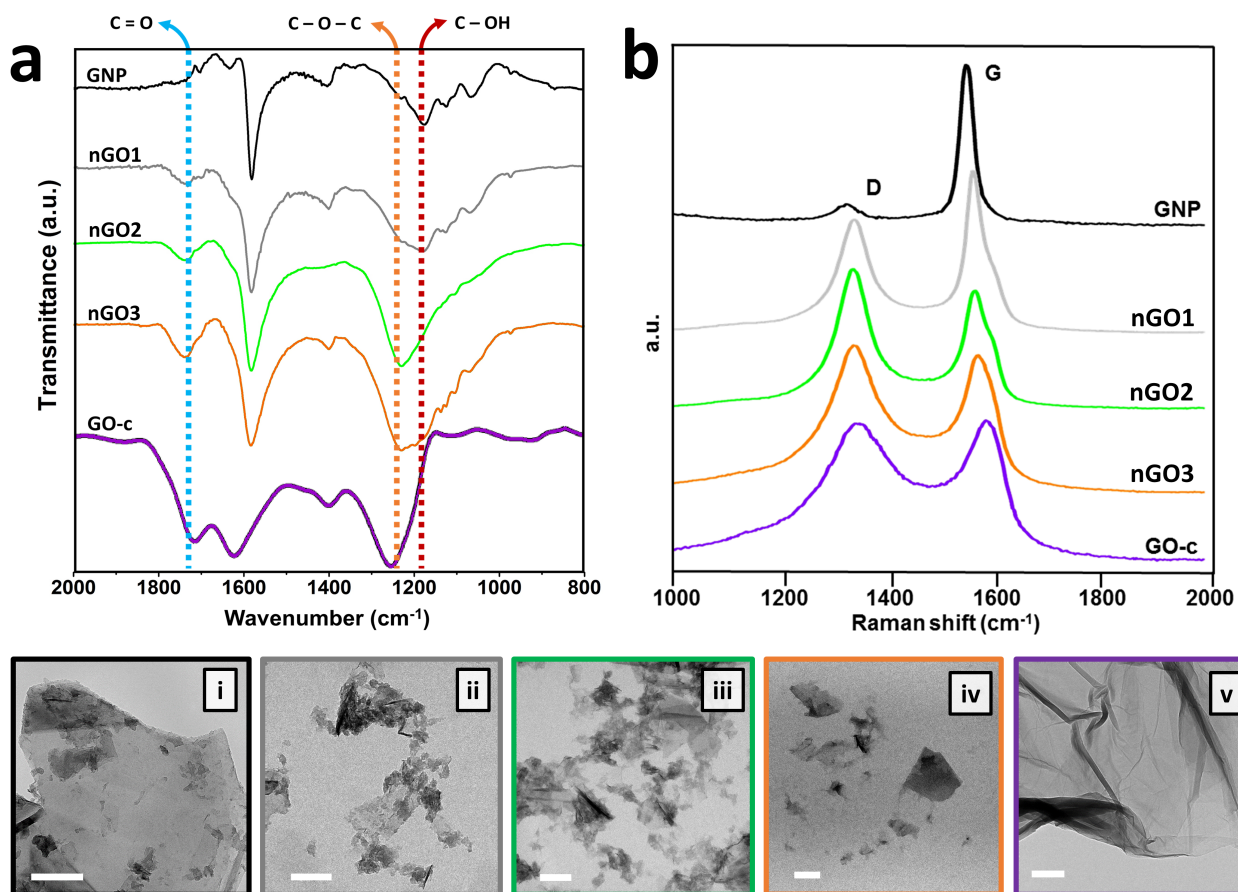


Figure 1. (a) FTIR spectra, (b) Raman spectra, (i-v) TEM images of GNP, *nGO1*, *nGO2*, *nGO3* and *GO-c* samples, respectively. Scale bar is 200 nm.

The *nGOx* samples were characterized by a multi-technique approach and **Table 1** summarizes the obtained results.

Table 1. Summary of the characterization results for the different GFM and complete DMEM.

	<i>EDX</i>	<i>Raman</i>		<i>DLS</i>				<i>LDME</i>	
	C/O atomic ratio	I_D/I_G	<i>L</i> (nm)	d_{HD} (H ₂ O, nm)	<i>PDI</i> H ₂ O	d_{HD} (DMEM, nm)	<i>PDI</i> DMEM	ζ -potential (H ₂ O, mV)	ζ -potential (DMEM, mV)
<i>GNP</i>	22.7 ± 4.1	0.14	11.8	-	-	-	-	-	-
<i>nGO1</i>	5.6 ± 0.3	0.75	2.8	242 ± 2	0.20 ± 0.03	834 ± 146	0.42 ± 0.01	-59.2 ± 1.2	-8.0 ± 0.8
<i>nGO2</i>	3.8 ± 0.3	1.23	2.6	200 ± 1	0.17 ± 0.02	609 ± 65	0.36 ± 0.04	-52.0 ± 0.8	-8.2 ± 0.9
<i>nGO3</i>	2.0 ± 0.2	1.11	2.0	224 ± 1	0.20 ± 0.01	212 ± 83	1.00 ± 0.00	-64.7 ± 0.6	-8.9 ± 0.7
<i>GO-c</i>	3.3 ± 0.3	1.04	1.7	1316 ± 80	0.49 ± 0.09	1341 ± 183	0.71 ± 0.10	-51.6 ± 2.0	-7.5 ± 0.8
<i>complete DMEM</i>	-	-	-	-	-	18.1 ± 0.1	0.39 ± 0.01	-	-5.3 ± 0.9

The energy dispersive X-ray spectroscopy (EDX) analysis indicated a progressive decrease of nGO_x C/O atomic ratio with increasing amounts of permanganate oxidizing agent. The nature and the content of the oxygen-containing groups were assessed by FTIR spectroscopy (**Figure 1a**). FTIR analysis showed that the relative amount of hydroxyl, epoxide and carboxyl groups changed with the final oxidation degree of nGO. For example, the amount of hydroxyl groups was higher at lower oxidation degree, while epoxy groups prevailed at higher oxidation degrees. The presence of the peaks characteristic for hydroxyl, epoxy and carboxyl groups denotes that oxidation occurred on both edges and basal planes of the platelets [56]. We evaluated the intensities and the areas of defect (D) and graphene-like (G) bands by Raman analysis (**Figure 1b**). Upon oxidation, a progressive increase of the intensity ratio between the D-band and the G-band (I_D/I_G) was found going from GNP to nGO_2 (**Table 1**), demonstrating a progressive breaking of the symmetry of the graphene lattice, due to edge effects, sp^3 -defects, vacancy sites or grain boundaries. A slight reduction was observed for nGO_3 , as at higher oxidation degrees the graphene sheets start to be dominated by the structurally disordered areas [57]. The average aromatic cluster size (L), related to the size of extended aromatic domains left undamaged upon oxidation, was evaluated by the empirical equation:

$$L = 4 \frac{A_G}{A_D} \quad (1)$$

where A_G and A_D are the areas of the G and D bands, respectively [52]. As shown in **Table 1**, L decreased with increasing $KMnO_4$ dose, from 11.8 nm of GNP to 2.0 nm of nGO_3 .

The morphology of GNP, nGO_x and $GO-c$ was studied by bright field transmission electron microscopy (TEM), as shown in **Figure 1i-v**. Upon oxidation and ultrasonication, GNP large sheets are broken down in smaller nanoplatelets with lateral size between 200 and 500 nm. This effect can be mainly ascribed to the ultrasonication process, which is reported to fragmentize and separate graphene sheets [58]. The lateral size of $GO-c$ resulted to be about 5 times higher than the nGO_x particles (**Figure 1v**). Freshly prepared nGO_x and $GO-c$ dispersions (**Figure 2i-v**) were analysed by dynamic light scattering (DLS) in water as well as in DMEM supplemented with 10% Fetal Bovine Serum, named “complete DMEM”. The results are shown in **Figure 2a**. The average hydrodynamic diameter (d_{HD}) of all nGO_x water dispersions was about 200 nm, whereas d_{HD} of $GO-c$ was higher than 1.3 μm (see **Table 1**). The analyzed dispersions were stable, and no precipitate was observed, except for $GO-c$ in complete DMEM, where large aggregates can be visualized macroscopically (**Figure 2iv, right**).

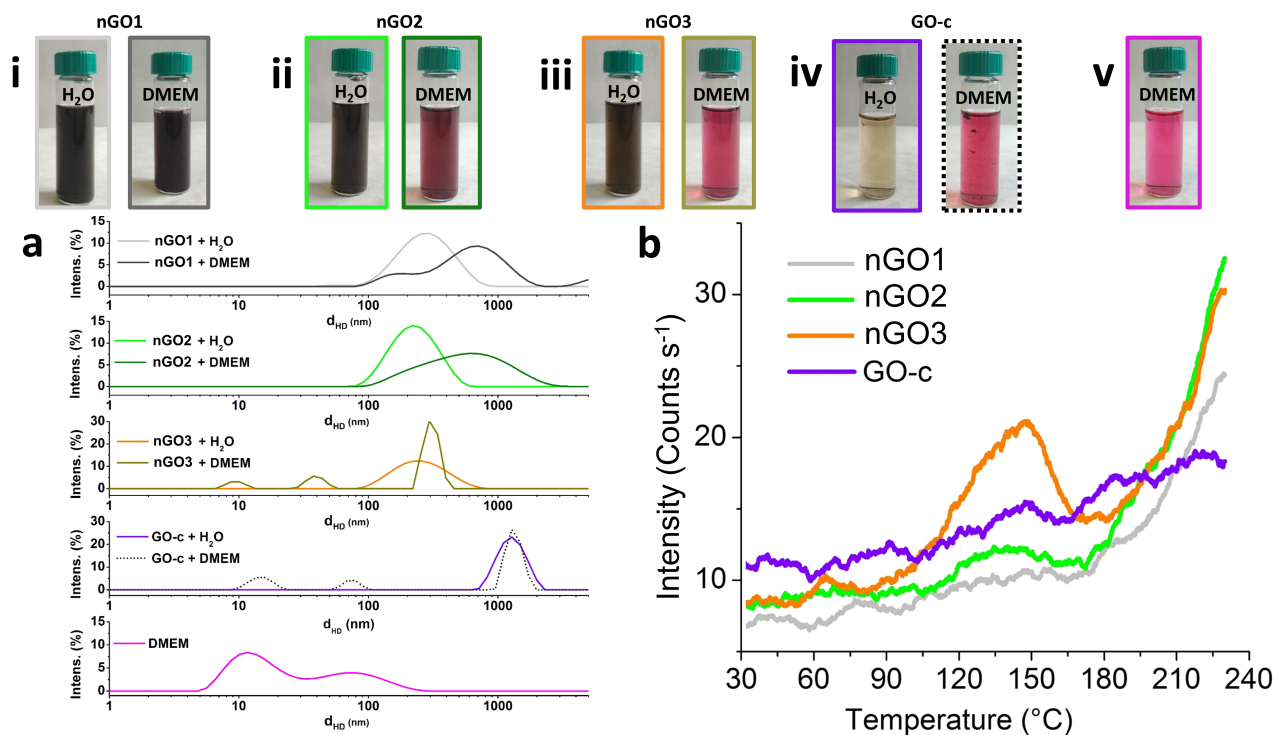


Figure 2. (i-iv) optical images of *nGOx* and *GO-c* samples dispersed in water or complete DMEM (50 $\mu\text{g}/\text{mL}$ concentration); (v) optical image of complete DMEM; (a) DLS results of *nGOx* and *GO-c* samples dispersed in water or complete DMEM; (b) TCL curves of *nGOx* and *GO-c*.

When dispersed in complete DMEM, *nGO1* and *nGO2* showed increased d_{HD} values, up to about 800 and 600 nm, respectively, due to the interactions of *nGO* platelets with the organic components of the cell medium. More specifically, for both *nGO1* and *nGO2* the d_{HD} increase could be associated to the well-known protein corona formation process, due to the presence of serum in the culture medium [44] [59] [60] (see the 3D animation in the **Supporting Information**), which endows *nGO* with a new biological fingerprint [61] [62].

For *nGO3* in complete DMEM, instead, this effect was not so relevant, as d_{HD} was in a range of about 200-300 nm, because of both its higher oxidation degree and the lower content of unmodified aromatic regions. Indeed, *nGO* mainly interacts with aromatic compounds, such as those present in complete DMEM, by means of π -interactions between hydrophobic regions of the protein and the carbon lattice [44] [63] [64]. Therefore, a reduced size of undamaged aromatic cluster areas, typical of higher oxidized GOs, prevents the formation of strong interactions with the organic component of complete DMEM. Coherently, peaks at 9.5 and 39.4 nm shown in the DLS curve of *nGO3* in complete DMEM, revealed the presence of free complete DMEM components, whose characteristic d_{HD} ranges between 5 and 200 nm, not interacting with *nGO*. Therefore, the coronation process was inhibited in case of *nGO3*. Moreover, a comparable DLS scattering distribution was noticed for *GO-c* in complete

DMEM, displaying characteristic d_{HD} values like those recorded for the free complete DMEM and *GO-c*, separately. The presence of the macroscopic *GO-c*/DMEM aggregates could not be detected because of DLS measurement limits.

A further indication on the interaction of the organic components of complete DMEM with *nGOx* and *GO-c* was provided by ζ -potential analysis with laser doppler micro-electrophoresis (LDME). As reported in **Table 1**, ζ -potential of complete DMEM resulted to be -5.3 mV, while those exhibited by *nGOx* and *GO-c* water dispersions were dramatically lower, ranging from about -50 to -65 mV. Once complete DMEM was mixed with *nGOx* and *GO-c*, the ζ -potential values of the obtained complex systems resulted much closer to that of the culture medium. This result confirms the occurrence of a strong interaction between the graphitic materials and complete DMEM, where the protein fraction of complete DMEM is covering nGO and GO particles, shielding almost completely their contribution to the ζ -potential [65]. Moreover, *nGO3* in complete DMEM showed the lowest ζ -potential value (-8.9 mV), demonstrating a lower screening effect by complete DMEM with respect to *nGO2* and *nGO1*, whose values were -8.2 and -8.0 mV, respectively. *GO-c* in complete DMEM exhibited the highest ζ -potential value (-7.5 mV), meaning that a more efficient interaction occurs in this system, whose main outcome are the macroscopic aggregates discussed above.

General conclusions can be drawn about the colloidal stability of *nGOx* and *GO-c* dispersions. As known [66], a nano-particles dispersion should exhibit a value below -30mV to be stable, with no aggregate formed. The increased ζ -potential values associated to nGO/DMEM dispersions, indicate that the observed stability of *nGO1* and *nGO2* dispersions was due to the steric repulsion between non-covalent protein corona shells decorating the nanoparticles surface, which prevailed over the electrostatic repulsion between nGO particles which took place in water. On the other hand, the highly oxidized surface of *nGO3* hindered the formation of GO-protein corona complexes. The observed stability of *nGO3* in DMEM is mainly due to the small size and the interaction between *nGO3* and polar organic components of the cell medium [63]. This resulted in a moderate increase in dimension and standard deviation of the nanoparticles (**Table 1**) [61] [62]. This view was also corroborated by ζ -potential analysis of *nGO3* in DMEM, which exhibited the lowest value, since the ζ -potential value was largely affected by the surface charge of *nGO3* nanoparticles. In this respect, the size of the *nGO3* sheets is of a paramount importance for the colloidal stability of the DMEM dispersion. Indeed, *GO-c* showed an oxidation degree comparable to that of *nGO2* (**Table 1**), however it did form microscopic aggregates, as the coronation process results in large particles with dramatically reduced colloidal stability in DMEM.

nGOx and *GO-c* samples were analyzed by thermochemiluminescence (TCL), to assess the effect of oxidation conditions on the formation of radical species. It is known that freshly prepared GO exhibits

a large number of π -conjugated carbon radicals able to directly initiate the long-lasting visible chemiluminescence (CL) reactions [67]. Typically, distinct light emission arises from the thermal decomposition of unstable peroxy radicals formed upon oxidation of organic materials. Therefore, TCL was measured by temperature-ramping experiments under nitrogen. The TCL curves are reported in **Figure 2b** and show no light emission for *nGO1* and *nGO2*, as well as for *GO-c*, while for *nGO3* a broad peak with a maximum at about 145 °C was evident. This result suggests that the carbon radicals generated upon GNP oxidation are partially converted into peroxidic species when more drastic oxidation conditions are used (i.e. *nGO3*). These reactive species undergo thermal decomposition in nitrogen, resulting in CL emission. It is likely that reactive oxygen species (ROS) formed on the graphene platelets can initiate radical reactions, eventually resulting in cell death [61], as reported in the next section.

2.2. Effects of nGO internalization on cell viability

To the best of our knowledge, the oxidized form of this commercial GNP has never been studied for cellular uptake applications. To investigate the effects on cell viability of *nGOx* with different oxidation degrees (*nGO1*, *nGO2*, *nGO3*) and at different concentration (20, 50, and 100 $\mu\text{g/ml}$), we chose murine embryonic fibroblasts NIH-3T3 as a cell model to evaluate the cell response by MTT assay.

As shown in **Figure 3**, *nGO1* and *nGO2* at 20 $\mu\text{g/mL}$ did not exhibit cytotoxicity, and the cell viability rate was more than 70%. Above 50 $\mu\text{g/mL}$, these materials exhibited obvious cytotoxicity effects, with a consequent decrease of metabolic activity. As the *nGO1* and *nGO2* concentration increased, the survival rate of cells decreased correspondingly. MTT results provided evidence that *nGO3* was toxic to NIH-3T3 cells, independently of concentration.

However, as can be seen in the **Figure 3**, the viability of cells exposed to 100 $\mu\text{g/mL}$ of *nGO3* was higher than that relative to *nGO1* and *nGO2* at the same concentration. This outcome is in contrast with optical microscope observations (see **Figure 6**), which showed a round shape, typical of a dead cell. A similar observation has been reported in [68] [69], pointing out that the MTT compound can interfere with nGO. Therefore, the effects of *nGOx* on cell morphology was further evaluated by optical microscopy observations, for a deeper understanding of the interactions between *nGOx* and cells.

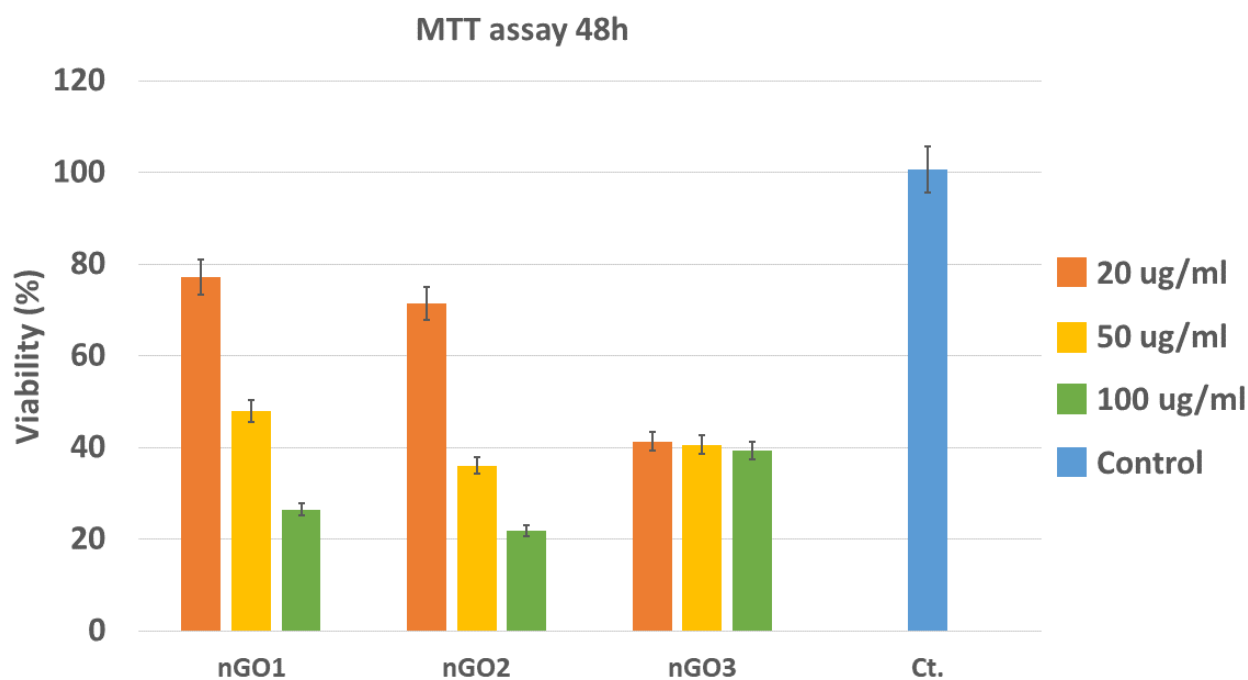


Figure 3. MTT cell viability assay. Effects of nGO1, nGO2, and nGO3 on mouse embryonic fibroblasts viability rate at different concentrations (20, 50 and 100 µg/ml), with respect to the control (Ct), represented by cells without nGO.

NIH-3T3 cells were seeded into Petri dishes and incubated at 37°C for 24 h with each of the *nGOx* water dispersions at three different concentrations, as summarized in **Table S1**. The samples were then observed under a conventional optical microscope at different exposure times, and **Figures 4, S1** and **S2** show the typical images recorded at 20, 50, and 100 µg/mL *nGOx* concentrations, respectively.

In case of 20 µg/mL (**Figure 4**) no significant effect after 3h incubation was observed. After 24 h, the cells with *nGO1* and *nGO2* presented a distinctive decoration of nGO clusters all around the nuclei (perinuclear region), as indicated by the red arrows. Correspondingly, the cells exposed to *nGO3* and *GO-c* showed no significant internalization. After 48 h, the effect of perinuclear decoration in the cells with *nGO1* and *nGO2* resulted in a darkening of the cytoplasm due to the massive internalization of the nanoparticles. This effect was more evident in the case of *nGO1*, due to its higher cytocompatibility. In fact, as reported above, *nGO1* showed relevant interactions with the organic components of the cell medium, endowing the nGO nanoparticles with a new biocompatible identity. It is likely that nanoparticles are located in specific districts such as lysosomes, mitochondrion, and endoplasm [9] and do not enter the nucleus due to the size of the nGO agglomerates that is larger than the functional diameter of the nuclear pores [70]. At the same time, the cell morphology appears regular with no evident effect on cell vitality and adhesion. In the same

picture, large floating nGO clusters can be observed, as the weak interactions between cell culture medium and the carbonaceous nanoparticles cause the nanoparticles to partly agglomerate. Nonetheless, the nGO uptake was not limited by the presence of the large nGO clusters outside cell membrane. Cells exposed to *nGO3* showed a morphology change from elongated to spherical, typical of cell death, with evident features of low vitality, as demonstrated in **Figure 3**. The morphology of cells exposed to *GO-c* resulted to be almost unaltered. Similar results were obtained at 50 µg/mL concentration (**Figure S1**). When exposed to *nGO1* and *nGO2*, the cells were able to proliferate until forming a biofilm covering the well growth area, in spite of a slight decrease of their metabolic activity, as reported in **Figure 3**. *nGO3* resulted to be cytotoxic also at 50 µg/ml, and only a slight nuclear decoration can be appreciated after 24h (see **Figure S1b3**). In case of *GO-c* no evidence of cell internalization was observed, since large scrolled-shaped sheets formed.

Concerning the concentration of 100 µg/mL (**Figure S2**) the image acquisition was difficult due to the presence of large aggregates for all tested GO samples. However, the elongated morphology of the cells was preserved in case of *nGO1* and *nGO2* even after 48 h incubation, while the viability decreased as pointed out by MTT assay. On the contrary, *nGO3* and *GO-c* exhibited significant evidences of cell death after 48h, such as morphology changes and cells floating in the medium (**Figure S2c3-c4**).

A conventional live/dead viability/cytotoxicity assay kit, reported in Supporting Information (**Figures S3-S5**), also tested the biocompatibility of nano-graphene at different oxidation degrees and different concentrations.

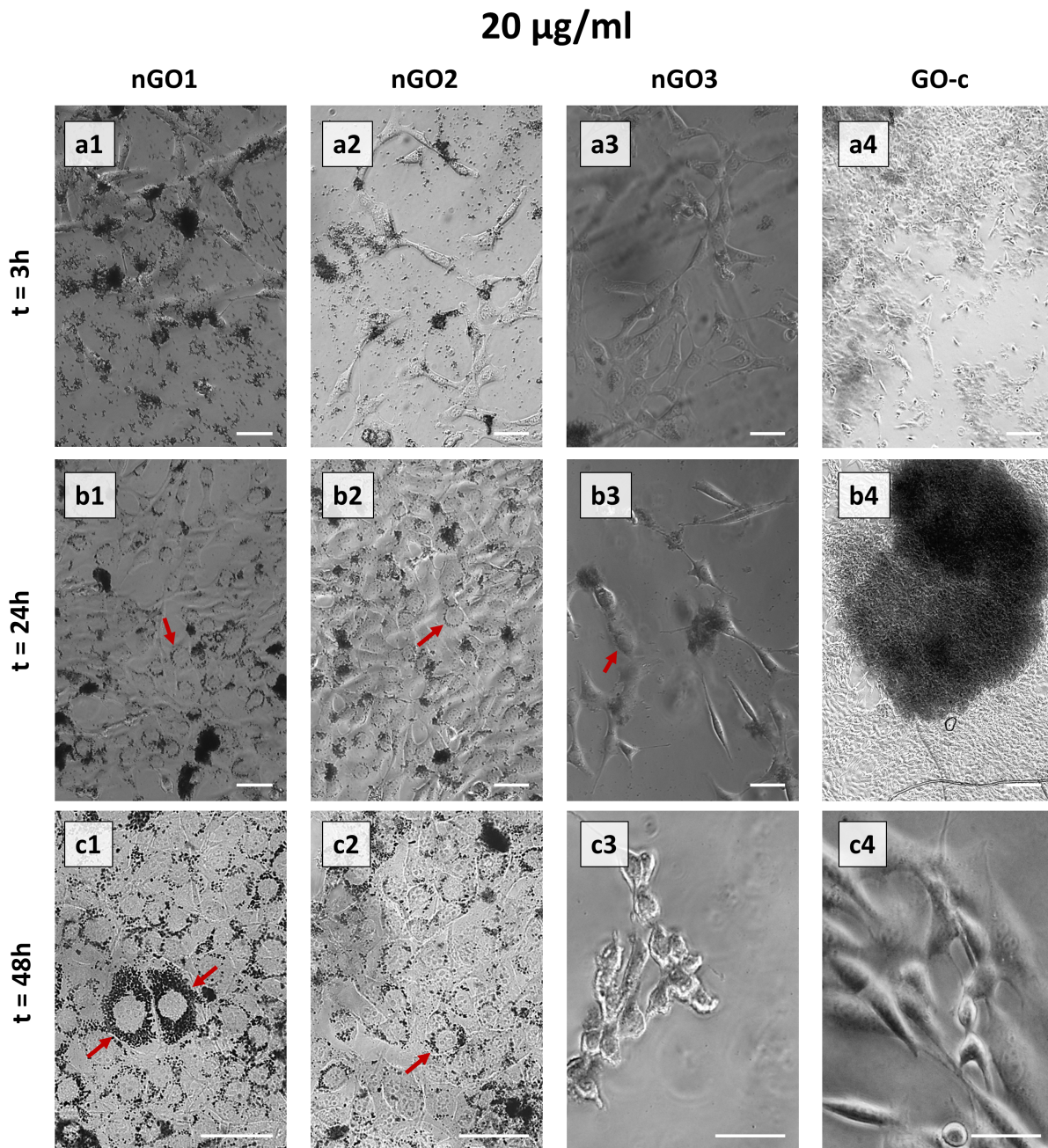


Figure 4 Optical microscopy images of cells incubated with different nGO materials (*nGO1*, *nGO2*, *nGO3*, *GO-c*) at a concentration of 20 $\mu\text{g}/\text{mL}$ at different time points (3h, 24h, 48h). The red arrows indicate the perinuclear decoration effect corresponding to the particles internalization. The scale bar is 50 μm long in a1-a3), b1-b3), c1-c3). The scale bar is 200 μm long in a4), b4) while is 20 μm long in c4).

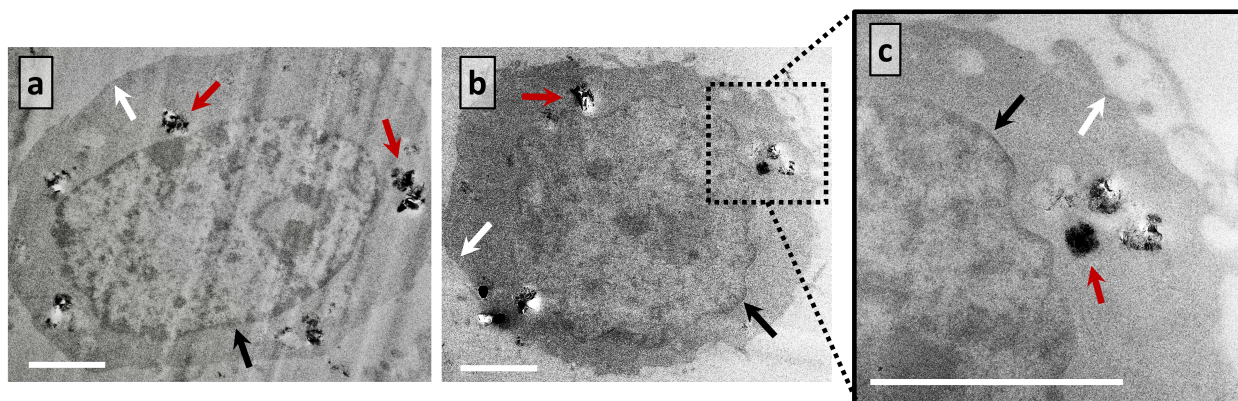


Figure 5. Bright field TEM pictures of perinuclear decoration of *nGO2* inside NIH-3T3 cells, after 48h at a concentration of 50 $\mu\text{g/ml}$. White arrows indicate the cytoplasmic membrane, black arrows indicate the nuclear membrane and red arrows indicate *nGO2* particles. In a, b and c, scale bars are 2 μm . c is the magnification of the dashed square in b.

Bright field TEM observations of ultrathin NIH-3T3 cell sections corroborated the results obtained by optical microscopy. **Figure 5** shows TEM images of the ultrastructural features of the NIH fibroblasts exposed to *nGO2* at a concentration of 50 $\mu\text{g/ml}$ for 48h. *nGO* was indeed internalized by cells and mainly located inside cytoplasm, around cell nucleus. In **Figure 5c** is possible to appreciate the *nGO* localization within the cytoplasm, as well as the dimension of the nanoparticle (300 nm) and the relative distance from the cell nucleus (150 nm). We also observed that, as the culture time increased, the amount of *nGO2* inside NIH cells increased accordingly, and lots of *nGO* black particles appeared to stand in the cell cytoplasm around cell nucleus. Indeed, in order to evaluate cell internalization at longer exposure times we incubated the cells with *nGO2* at a concentration of 50 $\mu\text{g/mL}$ up to 96h. More massive cellular uptake was noticed, while cell adhesion and shape were preserved due to the *nGO* coronation process, which reduced the NIH-3T3 cellular morphological damage (**Figures 6a-c**).

In summary, bright field microscopy observations on live cells demonstrated the biocompatibility of low oxidized *nGO* in NIH-3T3 fibroblasts, probably due to the *nGO* coronation by the proteins of serum-containing cell culture medium [59]. On the other hand, highly oxidized *nGO* did not show the same affinity with the complete DMEM components, therefore its cell internalization as well as cytocompatibility are significantly impaired.

Very importantly, lateral size dramatically affects biocompatibility of *GO*. Indeed, *GO-c*, which was 5 times larger than *nGOx* samples, massively aggregated in presence of complete DMEM. Moreover, it induced cell death, impairing cell adhesion, and no evidence of cell uptake was observed. Even if

GO-c did not interact directly with cells, cell death can be ascribed to the cell starvation due to the uptake of nutrients by the large carbonaceous aggregates standing outside the cell membrane. [71].

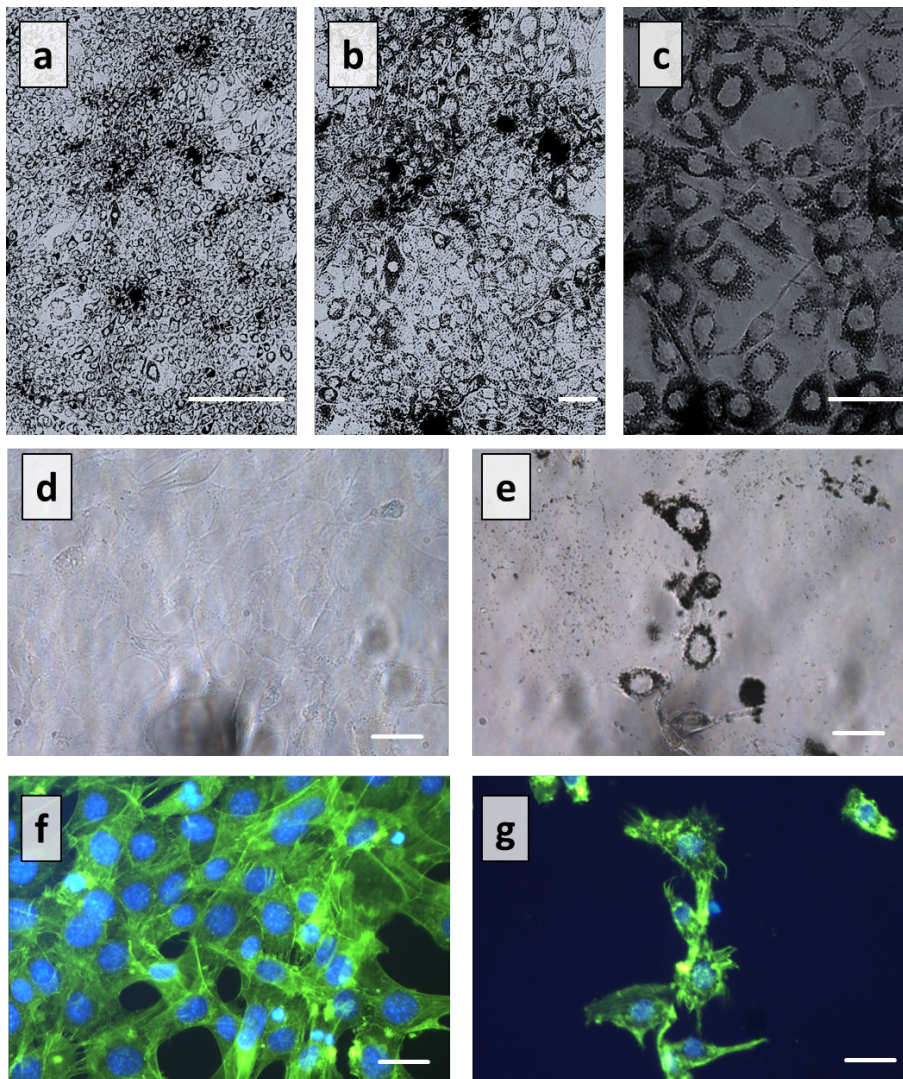


Figure 6. Optical microscope images (a, b, c) of cells incubated with *nGO2* at 50 µg/mL and observed 96 h after seeding, under different magnifications. The scale bars are 200 µm in a), and 40 µm in b) and c). Optical microscope images under bright field and fluorescence visualization of (d, f) control cells without *nGO* and (e, g) cells incubated with *nGO2* at a concentration of 20 µg/mL, all fixed 72 h after seeding and stained by immunofluorescence kit in order to observe the cell morphology. The nuclei are labeled blue while the actin filaments are labeled green. The scale bars are 25 µm.

As a further confirmation of the massive cellular uptake of *nGO*, leading to a peculiar accumulation of the particles into the cytoplasm volume, we evaluated also the cell morphology and the cytoskeleton assembly by staining the nuclei and the actin filament (see details in the **Experimental Section**). **Figure 6** shows the typical bright field and fluorescence images for a control sample without *nGO* (**Figure 6d, f**), and for cells incubated with *nGO2* at 20 µg/mL (**Figure 6e, g**), all fixed

and labeled 72 h after seeding. The morphology of cells exposed to *nGO2*, appeared clearly perturbed compared to the control. The nucleus (labeled blue) was smaller and the actin filaments (labeled in green) were unstructured and poorly polymerized, probably due to the mechanical stress induced by the nGO internalized by the cells. The above reported outcomes suggest that *nGO1* and *nGO2* DMEM dispersions can be suitably used as nano-vectors for drug delivery applications, since exhibit low cytotoxicity and a significant internalization rate in cell cytoplasm [72].

2.3. Quantitative evaluation of nGO uptake in live cells

A preliminary assessment of the cell thickness variation before and after nGO exposure was performed by a standard profilometer (see **Supporting Information, Figure S6**). For a quantitative evaluation of volume changes during nGO uptake in live cells, we used a DH system [73]. The technique allowed us to avoid the time-consuming and detrimental procedures usually employed for evaluating the GFM internalization, such as transmission electron microscopy, which requires cell fixing and laborious sample preparation. Moreover, DH is a label-free imaging technique based on a microscopy tool able to provide quantitative phase contrast images of the live cells, thus avoiding, also in this case, time-consuming sample preparations. Herein, we focused our attention on the cell uptake mechanism in case of *nGO2* at 50 µg/ml concentration, since the latter appeared to be the best candidate for highly efficient drug delivery. Indeed, it possess the best compromise between exposed specific surface area (SSA) in aqueous media and content of oxygen-containing groups. Moreover, Castaldo et al. [52] demonstrated its ability to adsorb an aromatic dye, methylene blue, which can be considered as a model drug [53] [54] [55].

The sample preparation for the DH analysis is outlined in **Figure 7a**. **Figure 7b** shows the DH setup based on a Mach-Zehnder interferometer with a CW solid state laser source emitting at 532 nm (max power 400 mW) that is split into two beams, the object and the reference. The object beam traverses the sample (i.e. the cells) and, after magnification by a 60× water immersion microscope objective (MO) (N.A. 1.2), recombines with the reference beam by the cube beam splitter (BS) and generates an interference fringe pattern (i.e. hologram), such as the one shown in **Figure 7c**.

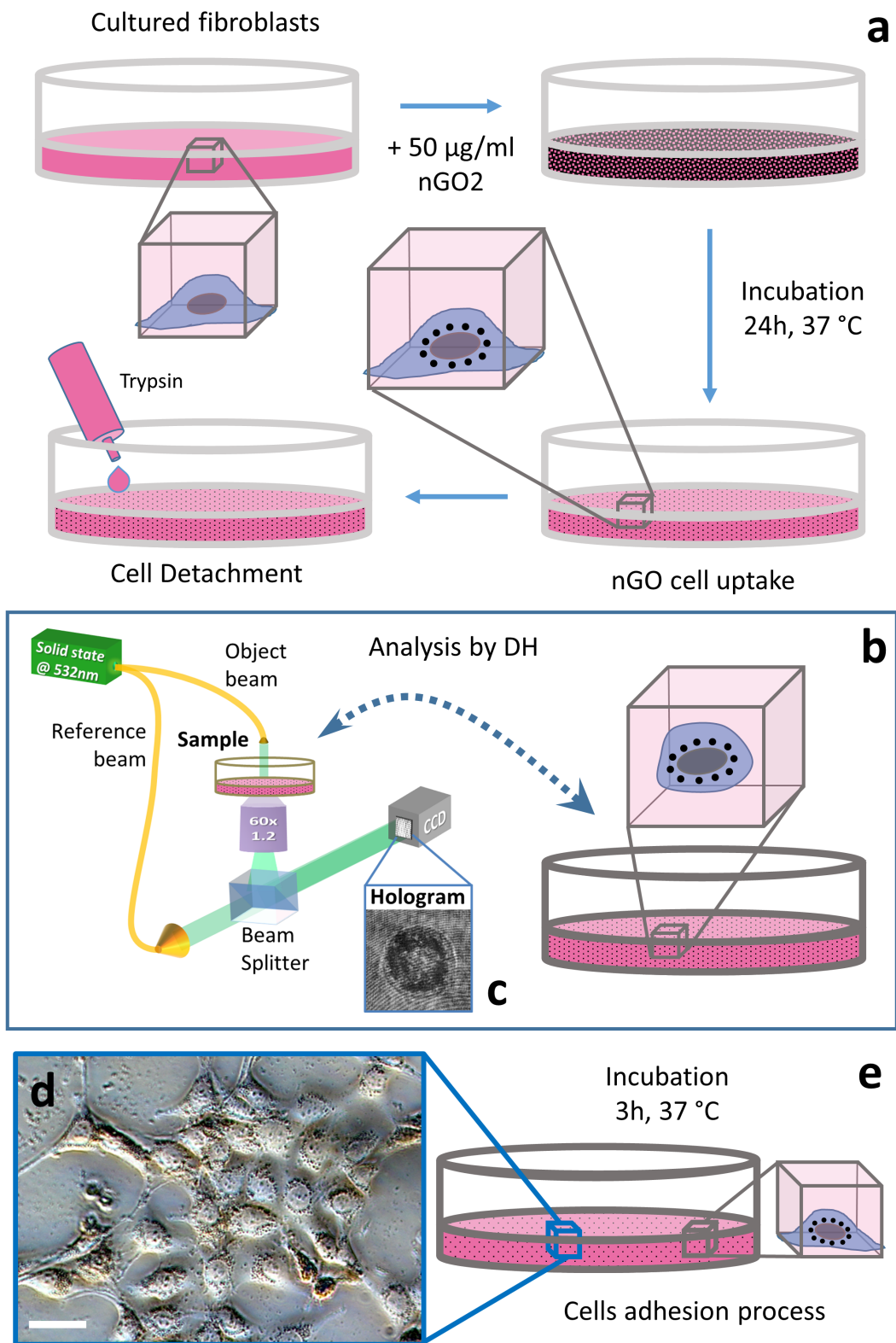


Figure 7. Schematic views of (a) the cell sample preparation for DH analysis and of (b) the DH setup; (c) typical interference pattern recorded by the camera of the DH system. (d) Optical microscope image of the cells after 24 h incubation with 50 $\mu\text{g/ml}$, (e) detached by trypsin and new 3h long incubation in standard medium.

The cells analysed in the DH system were cultured in a glass WillCo-dish, and a conventional CCD camera was used to record the intensity pattern of the hologram. The latter, after numerical processing, yielded access to the phase shift information $\Delta\varphi$, arising from the difference in refractive index between the specimen and the surrounding medium [74]:

$$\Delta\varphi(x,y) = \frac{2\pi}{\lambda} [n_c(x,y) - n_m] h(x,y) \quad (2)$$

where λ is the laser wavelength, $n_c(x,y)$ is the spatial refractive index of the cell, n_m is the refractive index of the surrounding solution, and h is the cell height at position (x,y) in the field of view. It is well known that it is not possible to evaluate the cell height without decoupling the contribution of the refractive index of the involved materials, thus we can measure phase volume changes only.

The cells were seeded in a Petri dish, and after 24 h incubation, a complete DMEM suspension of *nGO2* (ultrasonicated, 50 $\mu\text{g}/\text{mL}$) was added and incubated for another cycle of 24 h. Afterwards, the cells were detached by incubation with trypsin – EDTA and seeded in the WillCo-dish to be mounted into the DH system. We analysed the cells under both suspended and adherent conditions by recording the holograms just after seeding the cells into the WillCo-dish. Once DH analysis was completed, the cells were let to adhere on the bottom surface of the Petri dish in the successive three hours. By conventional optical microscopy, we observed that the nanoparticles clearly filled the cytoplasm and maintained the perinuclear localization (**Figure 7d-e**), analogously to the experiments shown above (**Figure 4**), where the cells were not detached after nGO uptake. This demonstrates that the cells, even after trypsinization, preserve the internalized material together with the adhesion functionalities. **Figure 8a** shows the reconstructed phase map in case of adherent cells, where the boundaries of the nuclei (see the red arrows) are clearly visible due to the highly sensitive detection of the refractive index variation between the cytoplasm and the nucleus, without the use of labelling procedures.

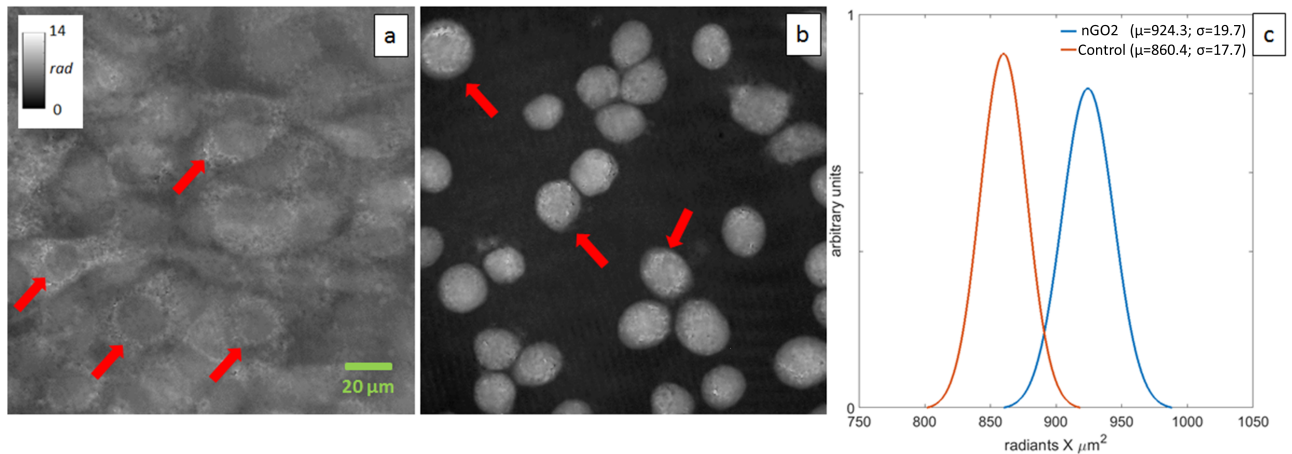


Figure 8. a) Quantitative phase images of adherent cells reveal perinuclear decoration after the *nGO2* internalization. b) Quantitative phase map of detached NIH-3T3 cells still highlights the perinuclear decorations after the *nGO2* internalization. c) Gaussian distributions of the phase volumes of cells before (red line) and after (blue line) the *nGO2* internalization.

The image shows also how the DH technique can show clearly the graininess of the *nGO2* internalized by the cytoplasm (see the red arrow). The phase map images show that the nanoparticles tend to fill the cytoplasm without penetrating the nucleus, in perfect agreement with the bright field images shown in **Figure S2b4**. However, the continuous overlap of adjacent cells in the field of view prevents an accurate image segmentation to select a single cell and evaluate the volume variation.

Figure 8b shows the typical reconstructed phase map in case of suspended cells. The arrow indicates clearly the cytoplasm regions filled by the internalized *nGO2*, thus demonstrating that the nanoparticles were still present into the cells even after detachment. DH has already been proved to be appropriate for studying suspended cells [75] and we evaluated here the cell volume V_{cell} according to the following formula:

$$V_{cell} = \sum_{(x,y) \in S} \Delta\varphi(x,y) \quad (3)$$

where S is the segmented region within each cell and $\Delta\varphi$ is the phase map reconstructed according to (2). **Figure 8c** reports the Gaussian distributions of the phase volumes of the cells before (red line) and after (blue line) the *nGO2* internalization, confirming the significant volume increase. We measured an average increase of 7% of phase volume per cell (with 0.14% as standard error estimation), corresponding to a total internalization of *nGO2* of about 5 $\mu\text{g/mL}$. We estimated this latter value by calculating an equivalent amount of internalized nGO if its nominal refractive index at our laser wavelength, $n_{nGO} = 2.4 - 1.0i$ [76], is used in equation (2), to calculate the nGO heights per each position (x,y) within the cell.

It is important to underline that the phase images in **Figure 8a-b** encode quantitative physical values of cells, within the image gray levels, according to the equation 2. Therefore, the phase volume shift reported in **Figure 8c** is the quantitative evaluation of the increased volume corresponding to the *nGO2* cells internalization.

3. Conclusion

We demonstrated how the mild oxidation of GNP followed by ultrasonication produces a material that promotes a highly efficient cellular uptake with massive internalization into the cytoplasm region. We focused our attention on nano-graphene oxide at intermediate oxidation degree (*nGO2*) that provides the best results in terms of biocompatibility and cellular uptake thanks to the best

combination of exposed surface area and functional groups. The results achieved in our research, in combination with the previous outcomes on the ability of this material to adsorb efficiently organic aromatic small molecules, definitively launches *nano graphene oxide* toward a promising application for highly efficient drug delivery. Moreover, we showed for the first time the ability of DH to evaluate the cell volume variation after nGO internalization in live cells, thus avoiding detrimental and time-consuming procedures such as those employed for electron-based microscopy. In this framework, we demonstrate that DH microscopy is useful for rapid, non-invasive and quantitative investigation of the morphometric evolution of cells under nanomaterials exposure, whereas traditional techniques, such as the use of fluorophore for the quenching and the MTT assay for the cell viability can interfere with nanoparticles.

Our results show that the label-free character of the technique would allow biologists to perform systematic and reliable studies on cell toxicology processes induced by nanomaterials, and to extract the biophysical parameters such as cell volume, projected surface area, cell thickness and dry mass from quantitative phase images without time-consuming calibration procedures. Future studies will be extended to monitoring tumor and neurons cells uptake of nGO functionalized with anti-cancer drugs, as well as methylene blue, in order to select the best conditions, in terms of concentration, uptake rate and dynamic release, for targeted therapy for cancer or neurodegenerative disorders, in the new paradigm of *personalized medicine* in which drugs are specifically tailored [17] [30].

4. Experimental Section

Nanoparticles: Graphene Nanoplatelets (GNP, grade C, average lateral dimensions 2 μm , XG Science - Lansing, MI, USA). Commercial water dispersed GO (*GO-c*) and all reagents and solvents were purchased by Sigma Aldrich (Milan, Italy) and used without further purification.

Oxidation procedure: nGO samples at three different oxidation degrees were synthesized according to a modified Hummers method [77]. 1g of GNP was stirred for 30 min in 25 mL of a 96% H_2SO_4 solution in ice bath. Then, depending on the envisaged oxidation degree, 1, 2, or 3 wt equivalents of KMnO_4 , with respect to the amount of GNP, were progressively added. During this operation, the temperature of the ice bath was kept below 25 °C. For the successive two hours, the temperature was set at 35 °C. Afterward, 45 mL of DI water were gently added to the stirring mixture, while the temperature of the bath was raised at 70 °C. After 15 minutes, 100 mL of H_2O_2 water solution (3 wt%) were transferred in the suspension, and stirred for one more hour. Then the precipitate was collected by means of centrifugation. The resulting black muddy paste was dispersed in 140 mL of 5 wt% HCl solution, in order to remove the contaminating salts. The resulting dispersion was stirred and centrifuged, and the precipitate was washed in DI water and centrifuged several times, until

neutrality. To ensure the homogeneous dispersion of the oxidized nanoparticles, each sample was diluted to 4 mg/mL of nGO and subject to ultrasonication (2 hours, 25% amplitude, 30 seconds ON/30 seconds OFF). Depending on the wt equivalent of KMnO_4 , and on the obtained oxidation degree, the samples were coded as *nGO1*, *nGO2* and *nGO3*, respectively lower, intermediate and higher oxidation degree.

Characterization Techniques: Elemental analysis on GNP, dried *nGOx* and *GO-c* samples was performed through energy dispersive X-ray spectroscopy (EDX) using a FEI Quanta 200 FEG SEM equipped with an Oxford Inca Energy System 250 and an Inca-X-act LN_2 -free analytical silicon drift detector. The analysis was performed at 30 kV acceleration voltage. The reported results and standard deviation values are obtained from three measurements conducted on different areas of each sample. Morphological analysis of GNP, nGO and *GO-c* samples was conducted by bright field transmission electron microscopy (TEM) using a FEI Tecnai G12 Spirit Twin (LaB_6 source) at 120 kV acceleration voltage equipped with a FEI Eagle 4k CCD camera. The samples were prepared by immersing carbon coated TEM copper grids in 1 mg/mL *nGOx* and *GO-c* water dispersions and in a 1 mg/mL N,N-dimethylformamide (DMF) GNP dispersion.

GNP, *nGOx* and *GO-c* Raman spectra were collected by a Horiba-Jobin Yvon Aramis Raman spectrometer operating with a diode laser excitation source limiting at 532 nm and a grating with 1200 grooves/mm. The 180° back-scattered radiation was collected by an Olympus metallurgical objective (MPlan 50X, NA = 0.50) and with confocal and slit apertures both set to 400 μm . The radiation was focused onto a Peltier-cooled CCD detector (Synapse Mod. 354308) in the Raman-shift range $2000\text{--}1000\text{ cm}^{-1}$. Spectral deconvolution was performed by using Grams/8.0AI software.

Fourier transform infrared spectroscopy (FTIR) was performed on GNP, dried *nGOx* and *GO-c* samples, in order to investigate the oxygen-containing functional groups in GO samples. Spectra were recorded with a Perkin Elmer Spectrum One FTIR spectrometer using a resolution of 4 cm^{-1} and 32 scan collections.

Thermochemiluminescence (TCL) experiments were performed by means of a Lumipol 3 luminometer in nitrogen flow. The samples were obtained by film casting 0.5 mL of *nGOx* water dispersions onto an aluminium pan. Each sample was heated from 30 to $230\text{ }^\circ\text{C}$ at $5\text{ }^\circ\text{C min}^{-1}$ and then cooled to room temperature.

Water- and DMEM-based nGO and *GO-c* dispersions at fixed concentration ($50\text{ }\mu\text{g/mL}$) were analysed through dynamic light scattering (DLS) and laser doppler micro-electrophoresis (LDME). Hydrodynamic diameters (d_{HD}) and ζ -potentials were measured using a Zetasizer Nano ZS (Malvern Instruments) at scattering angle of 173° . Measurements were performed in triplicate at $25\text{ }^\circ\text{C}$ for water based samples and at $23\text{ }^\circ\text{C}$ for DMEM based samples. To ensure the homogenous distribution of the

nanoparticles in the cell culture medium (complete DMEM) once exposed to the *nGO*_x dispersions, the latter were previously sonicated in an ultrasonication bath. Then, the obtained mixtures underwent a mild mechanical agitation in order to maintain the uniformity of the distribution of the particles within the medium.

Cell culture: Murine embryonic fibroblasts NIH-3T3 were chosen to analyze the effects of nGO at different oxidation degrees *in-vitro*. NIH-3T3 were grown in Dulbecco's Modified Eagle Medium supplemented with 10% Fetal Bovine Serum (both Life Technologies, Carlsbad, CA, USA), 2 mM L-glutamine (Sigma, St. Louis, MO), and 100 U/ml penicillin, 100 µg/ml streptomycin. Then, fibroblasts were seeded at cell density of 5×10^4 cells/ml in a 35 mm petri dish, and incubated at 37°C and in humidified 5% CO₂ atmosphere in an incubator (Esco). In order to investigate nGO cytotoxicity, varying amounts (20, 50, and 100 µg/ml) of nGO at different oxidation degrees were added in the complete DMEM medium. For comparison, the same analysis was performed with *GO-c*. Then, the cell culture were monitored at different time points, at 3h, 24h, and 48h, respectively. Images were collected with phase contrast microscope (Axio Zeiss Vert). Each experiment was repeated in triplicate.

MTT cell viability assay In order to investigate the cytotoxicity of nGO *in vitro*, we chose mouse embryonic fibroblast cell (NIH) as the target cells to evaluate the cell viability and proliferation by MTT assays according to manufacturer's procedures (Vybrant® MTT Cell Proliferation Assay Kit, Thermo Fisher Scientific). Cells were seeded at cell density of 18,000 cells/ml in the 8-well plate and incubated in a humidified 5% CO₂ balanced air incubator at 37°C for 24 h. Except from control wells, in the remaining wells nGO1, nGO2, and nGO3 were added to the medium at the final concentrations of 20, 50, and 100 µg/mL. The cells were cultured until 48h, then MTT assay was performed according to the manufacturer's protocols, and the absorbency was measured using the spectrophotometer (Beckman Coulter, DU730). The cell viability was calculated by the following equation:

$$\text{Viability (\%)} = [A_{540}(\text{sample}) / A_{540}(\text{control})] \times 100 \quad (4)$$

where $A_{540}(\text{sample})$ is absorbance intensity at 540 nm in the presence of nGO, and $A_{540}(\text{control})$ is absorbance intensity at 540 nm in the absence of nGO.

Sample preparation for TEM analysis: The perinuclear decoration of nGO inside the cytoplasm was validated by bright field TEM analysis. The sample preparation consisted in seeding NIH-3T3 at cell density of 50,000 cells/mL in a 35 mm Petri dish, treated with 50 µg/mL nGO2 and cultured in a humidified 5% CO₂ balanced air incubator at 37°C for 48 h. Then, the cells were fixed with 2.5%

glutaraldehyde solution and embedded with epoxy resin (Epoxy-Embedding kit 45359 SIGMA-ALDRICH). Ultrathin sections of the embedded samples were prepared with a Leica UC7 ultramicrotome (nominal thickness 100 nm) and collected on TEM copper grids. TEM observations were performed in bright field mode using an acceleration voltage of 120 kV.

Immunofluorescence assay: For fluorescence staining, cells were fixed with 4% paraformaldehyde in PBS for 15 min at room temperature, permeabilized with 0.1% Triton X-100 and labelled with Alexa fluor 488 phalloidin (Sigma) to reveal the actin filaments. The nuclei were stained with blue fluorescent Hoechst 33342 dye, trihydrochloride trihydrate (Molecular Probes Invitrogen).


ASSOCIATED CONTENT

Supporting Information

Optical microscopy images of cells incubated with *nGO1*, *nGO2*, *nGO3* and *GO-c* at concentration of 50 and 100 µg/mL and different time points (3h, 24h, 48h), cell viability assay (calcein/ethidium homodimer), profilometer analysis, and 3D animation of nGO cell uptake.

Notes The authors declare no competing financial interest

ACKNOWLEDGMENTS

The authors acknowledge the  EU funding within the Horizon 2020 Program, under the FET-OPEN Project “SensApp”, Grant Agreement n.829104. The authors acknowledge Dr. Luigi Leone and Dr. Ida Romano for the use of the spectrophotometer facility.

Martina Mugnano, Giuseppe Cesare Lama and Rachele Castaldo contributed equally to this work.

REFERENCES

-
- [1] Novoselov, K.S.; Geim, A.K.; Morozov, S.V.; Jiang, D.; Zhang, Y.; Dubonos, S.V.; Grigorieva, I.V.; Firsov, A.A. Electric Field Effect in Atomically Thin Carbon Films *Science* **2004**, *306*, 666-669.
- [2] Kuila, T.; Bose, S.; Mishra, A.K.; Khanra, P.; Kim, N.H.; Lee, J.H. Chemical Functionalization of Graphene and its Applications *Progress in Materials Science* **2012**, *57*, 1061-1105.
- [3] Castaldo, R.; Avolio, R.; Cocca, M.; Gentile, G.; Errico, M.E.; Avella, M.; Carfagna, C.; Ambrogio, V. A Versatile Synthetic Approach Toward Hyper-Cross-Linked Styrene-based Polymers and Nanocomposites *Macromolecules* **2017**, *50*, 4132-4143.

-
- [4] Marotta, A.; Lama, G.C.; Ambrogi, V.; Cerruti, P.; Giamberini, M.; Gentile, G. Shape Memory Behavior of Liquid-Crystalline Elastomer/Graphene Oxide Nanocomposites *Composites Science and Technology* **2018**, *159*, 251-258.
- [5] Bonaccorso, F.; Sun, Z.; Hasan, T.; Ferrari, A.C. Graphene Photonics and Optoelectronics *Nature photonics* **2010**, *4*, 611-622.
- [6] Castaldo, R.; Lama, G.C.; Aprea, P.; Gentile, G.; Ambrogi, V.; Lavorgna, M.; Cerruti, P. Humidity-Driven Mechanical and Electrical Response of Graphene/Cloisite Hybrid Films *Advanced Functional Materials* **2019**, *29*, 1807744.
- [7] Dreyer, D.R.; Park, S.; Bielawski, C.W.; Ruoff, R.S. The Chemistry of Graphene Oxide *Chem. Soc. Rev.* **2010**, *39*, 228-240.
- [8] Singh, V.; Joung, D.; Zhai, L.; Das, S.; Khondaker, S.I.; Seal, S. Graphene Based Materials: Past, Present and Future *Progress in materials science* **2011**, *56*, 1178-1271.
- [9] Liu, Z.; Robinson, J.T.; Sun, X.; Dai, H. PEGylated Nanographene Oxide for Delivery of Water-Insoluble Cancer Drugs *Journal of the American Chemical Society* **2008**, *130*, 10876-10877.
- [10] Wang, K.; Ruan, J.; Song, H.; Zhang, J.; Wo, Y.; Guo, S.; Cui, D. Biocompatibility of Graphene Oxide *Nanoscale Research Letters* **2011**, *6*, 1-8.
- [11] Xu, Z.; Wang, S.; Li, Y.; Wang, M.; Shi, P.; Huang, X. Covalent Functionalization of Graphene Oxide with Biocompatible Poly (ethylene glycol) for Delivery of Paclitaxel *ACS applied materials & interfaces* **2014**, *6*, 17268- 17276.
- [12] Yin, F.; Gu, B.; Lin, Y.; Panwar, N.; Tjin, S.C.; Qu, J.; Lau, S.P.; Yong, K.T. Functionalized 2D Nanomaterials for Gene Delivery Applications *Coordination Chemistry Reviews* **2017**, *347*, 77-97.
- [13] Zhao, H.; Ding, R.; Zhao, X.; Li, Y.; Qu, L.; Pei, H.; Yildirimer, L.; Wu, Z.; Zhang, W. Graphene-based Nanomaterials for Drug and/or Gene Delivery, Bioimaging, and Tissue Engineering *Drug discovery today* **2017**, *22*, 1302-1317.
- [14] Liu, Y.; Yu, D.; Zeng, C.; Miao, Z.; Dai, L. Biocompatible Graphene Oxide-based Glucose Biosensors *Langmuir* **2010**, *26*, 6158-6160.
- [15] Chen, H.; Müller, M.B.; Gilmore, K.J.; Wallace, G.G.; Li, D. Mechanically Strong, Electrically Conductive, and Biocompatible Graphene Paper *Advanced Materials* **2008**, *20*, 3557-3561.
- [16] Shin, S.R.; Li, Y.C.; Jang, H.L.; Khoshakhlagh, P.; Akbari, M.; Nasajpour, A.; Zhang, Y.S.; Tamayol, A.; Khademhosseini, A. Graphene-based Materials for Tissue Engineering *Advanced drug delivery reviews* **2016**, *105*, 255-274.
- [17] Wang, Y.; Li, Z.; Wang, J.; Li, J.; Lin, Y. Graphene and Graphene Oxide: Biofunctionalization and Applications in Biotechnology *Trends in biotechnology* **2011**, *29*, 205-212.

-
- [18] Zhu, Y.; Murali, S.; Cai, W.; Li, X.; Suk, J.W.; Potts, J.R.; Ruoff, R.S. Graphene and Graphene Oxide: Synthesis, Properties, and Applications *Advanced materials* **2010**, *22*, 3906-3924.
- [19] Sahu, A.; Choi, W.I.; Lee, J.H.; Tae, G. Graphene Oxide Mediated Delivery of Methylene Blue for Combined Photodynamic and Photothermal Therapy *Biomaterials* **2013**, *34*, 6239-6248.
- [20] Ganguly, P.; Breen, A.; Pillai, S.C. Toxicity of Nanomaterials: Exposure, Pathways, Assessment, and Recent Advances *ACS Biomaterials Science & Engineering* **2018**, *4*, 2237-2275.
- [21] Zhang, J.; Chen, L.; Chen, J.; Zhang, Q.; Feng, J. Stability, Cellular Uptake, and in Vivo Tracking of Zwitterion Modified Graphene Oxide as a Drug Carrier *Langmuir* **2018**, *35*, 1495-1502.
- [22] Xu, M.; Zhu, J.; Wang, F.; Xiong, Y.; Wu, Y.; Wang, Q.; Weng, J.; Zhang, Z.; Chen, W.; Liu, S. Improved In Vitro and In Vivo Biocompatibility of Graphene Oxide through Surface Modification: Poly(Acrylic Acid)-Functionalization is Superior to PEGylation *ACS nano* **2016**, *10*, 3267-3281.
- [23] Hong, B.J.; Compton, O.C.; An, Z.; Eryazici, I.; Nguyen, S.T. Successful Stabilization of Graphene Oxide in Electrolyte Solutions: Enhancement of Biofunctionalization and Cellular Uptake *ACS nano* **2011**, *6*, 63-73.
- [24] Sasidharan, A.; Panchakarla, L.S.; Chandran, P.; Menon, D.; Nair, S.; Rao, C.N.R.; Koyakutty, M. Differential Nano-Bio Interactions and Toxicity Effects of Pristine Versus Functionalized Graphene *Nanoscale* **2011**, *3*, 2461-2464.
- [25] Wojtoniszak, M.; Chen, X.; Kalenczuk, R.J.; Wajda, A.; Łapczuk, J.; Kurzewski, M.; Drozdziak, M.; Chu, P.K.; Borowiak-Palen, E. Synthesis, Dispersion, and Cytocompatibility of Graphene Oxide and Reduced Graphene Oxide *Colloids and Surfaces B: Biointerfaces* **2012**, *89*, 79-85.
- [26] Zhang, S.; Yang, K.; Feng, L.; Liu, Z. In Vitro and In Vivo Behaviors of Dextran Functionalized Graphene *Carbon* **2011**, *49*, 4040-4049.
- [27] Pelin, M.; Fusco, L.; León, V.; Martín, C.; Criado, A.; Sosa, S.; Vázquez, E.; Tubaro, A.; Prato, M. Differential Cytotoxic Effects of Graphene and Graphene Oxide on Skin Keratinocytes *Scientific reports* **2017**, *7*, 40572.
- [28] Li, Y.; Yuan, H.; Von dem Bussche, A.; Creighton, M.; Hurt, R.H.; Kane, A.B.; Gao, H. Graphene Microsheets Enter Cells Through Spontaneous Membrane Penetration at Edge Asperities and Corner Sites *Proceedings of the National Academy of Sciences* **2013**, *110*, 12295-12300.
- [29] Seemork, J.; Sansureerungsikul, T.; Sathornsantikun, K.; Sinthusake, T.; Shigyou, K.; Tree-Udom, T.; Jiangchareon, B.; Chiablaem, K.; Lirdprapamongkol, K.; Svasti, J.; Hamada, T. Penetration of Oxidized Carbon Nanospheres Through Lipid Bilayer Membrane: Comparison to Graphene Oxide and Oxidized Carbon Nanotubes, and Effects of pH and Membrane Composition *ACS applied materials & interfaces* **2016**, *8*, 23549-23557.

-
- [30] Lu, N.; Wang, L.; Lv, M.; Tang, Z.; Fan, C. Graphene-based Nanomaterials in Biosystems *Nano Research*, **2019**, *12*, 247-264.
- [31] Sydlík, S.A.; Jhunjhunwala, S.; Webber, M.J.; Anderson, D.G.; Langer, R. In Vivo Compatibility of Graphene Oxide with Differing Oxidation States *ACS nano* **2015**, *9*, 3866-3874.
- [32] Li, R.; Guiney, L.M.; Chang, C.H.; Mansukhani, N.D.; Ji, Z.; Wang, X.; Nel, A.E. Surface Oxidation of Graphene Oxide Determines Membrane Damage, Lipid Peroxidation, and Cytotoxicity in Macrophages in a Pulmonary Toxicity Model *ACS nano* **2018**, *12*, 1390-1402.
- [33] Ouyang, S.; Hu, X.; Zhou, Q. Envelopment–Internalization Synergistic Effects and Metabolic Mechanisms of Graphene Oxide on Single-Cell *Chlorella Vulgaris* are Dependent on the Nanomaterial Particle Size *ACS applied materials & interfaces* **2015**, *7*, 18104-18112.
- [34] Yue, H.; Wei, W.; Yue, Z.; Wang, B.; Luo, N.; Gao, Y.; Ma, D.; Ma, G.; Su, Z. The Role of the Lateral Dimension of Graphene Oxide in the Regulation of Cellular Responses *Biomaterials* **2012**, *33*, 4013-4021.
- [35] Pinto, A.M.; Gonçalves, C.; Sousa, D.M.; Ferreira, A.R.; Moreira, J.A.; Gonçalves, I.C.; Magalhaes, F.D. Smaller Particle Size and Higher Oxidation Improves Biocompatibility of Graphene-based Materials *Carbon* **2016**, *99*, 318-329.
- [36] Zhang, H.; Peng, C.; Yang, J.; Lv, M.; Liu, R.; He, D.; Fan, C.; Huang, Q. Uniform Ultrasmall Graphene Oxide Nanosheets with Low Cytotoxicity and High Cellular Uptake *ACS applied materials & interfaces* **2013**, *5*, 1761-1767.
- [37] Chang, Y.; Yang, S.T.; Liu, J.H.; Dong, E.; Wang, Y.; Cao, A.; Liu, Y.; Wang, H. In Vitro Toxicity Evaluation of Graphene Oxide on A549 Cells *Toxicology letters* **2011**, *200*, 201-210.
- [38] Bianco, A.; Cheng, H.M.; Enoki, T.; Gogotsi, Y.; Hurt, R.H.; Koratkar, N.; Kyotani, T.; Monthieux, M.; Park, C.R.; Tascon, J.M.; Zhang, J. All in the Graphene Family—A Recommended Nomenclature for Two-Dimensional Carbon Materials *Carbon* **2013**, *65*, 1-6.
- [39] Jastrzębska, A.M.; Kurtycz, P.; Olszyna, A.R. Recent Advances in Graphene Family Materials Toxicity Investigations *Journal of Nanoparticle Research* **2012**, *14*, 1-21.
- [40] Seabra, A.B.; Paula, A.J.; de Lima, R.; Alves, O.L.; Durán, N. Nanotoxicity of Graphene and Graphene Oxide *Chemical research in toxicology* **2014**, *27*, 159-168.
- [41] Pinto, A.M.; Goncalves, I.C.; Magalhães, F.D. Graphene-based Materials Biocompatibility: a Review *Colloids and Surfaces B: Biointerfaces* **2013**, *111*, 188-202.
- [42] Zhang, X.; Hu, W.; Li, J.; Tao, L.; Wei, Y. A Comparative Study of Cellular Uptake and Cytotoxicity of Multi-Walled Carbon Nanotubes, Graphene Oxide, and Nanodiamond *Toxicology Research* **2012**, *1*, 62-68.

-
- [43] Rajesh, C.; Majumder, C.; Mizuseki, H.; Kawazoe, Y. A Theoretical Study on the Interaction of Aromatic Amino Acids with Graphene and Single Walled Carbon Nanotube *The Journal of chemical physics* **2009**, *130*, 124911-1 - 124911-6.
- [44] Syama, S.; Mohanan, P.V. Comprehensive Application of Graphene: Emphasis on Biomedical Concerns *Nano-Micro Letters*, **2019**, *11*, 1-31.
- [45] Mallineni, S.S.K.; Shannahan, J.; Raghavendra, A.J.; Rao, A.M.; Brown, J.M.; Podila, R. Biomolecular Interactions and Biological Responses of Emerging Two-Dimensional Materials and Aromatic Amino Acid Complexes *ACS applied materials & interfaces* **2016**, *8*, 16604-16611.
- [46] Mugnano, M.; Memmolo, P.; Miccio, L.; Grilli, S.; Merola, F.; Calabuig, A.; Bramanti, A.; Mazzon, E.; Ferraro, P. In Vitro Cytotoxicity Evaluation of Cadmium by Label-Free Holographic Microscopy *Journal of biophotonics* **2018**, *11*, e201800099.
- [47] Pham, H.V.; Bhaduri, B.; Tangella, K.; Best-Popescu, C.; Popescu, G. Real Time Blood Testing Using Quantitative Phase Imaging *PloS one* **2013**, *8*, 1-9.
- [48] Shaked, N.T.; Satterwhite, L.L.; Truskey, G.A.; Wax, A.P.; Telen, M.J. Quantitative Microscopy and Nanoscopy of Sickle Red Blood Cells Performed by Wide Field Digital Interferometry *Journal of biomedical optics* **2011**, *16*, 030506.
- [49] Mues, S.; Ketelhut, S.; Kemper, B.; Schnekenburger, J. Digital Holographic Microscopy Overcomes the Limitations of In Vitro Nanomaterial Cytotoxicity Testing *Quantitative Phase Imaging III, International Society for Optics and Photonics* **2017**, *10074*, 1007413.
- [50] Merola, F.; Memmolo, P.; Miccio, L.; Savoia, R.; Mugnano, M.; Fontana, A.; D'ippolito, G.; Sardo, A.; Iolascon, A.; Gambale, A.; Ferraro, P. Tomographic Flow Cytometry by Digital Holography *Light: Science & Applications* **2017**, *6*, e16241.
- [51] Villone; M.M.; Memmolo, P.; Merola, F.; Mugnano, M.; Miccio, L.; Maffettone, P.L.; Ferraro, P. Full-Angle Tomographic Phase Microscopy of Flowing Quasi-Spherical Cells *Lab Chip* **2018**, *18*, 126-131.
- [52] Castaldo, R.; Lama, G.C.; Aprea, P.; Gentile, G.; Lavorgna, M.; Ambrogi, V.; Cerruti, P. Effect of the Oxidation Degree on Self-Assembly, Adsorption and Barrier Properties of Nano-Graphene *Microporous and Mesoporous Materials* **2018**, *260*, 102-115.
- [53] Wischik, C.M.; Edwards, P.C.; Lai, R.Y.; Roth, M.; Harrington, C.R. Selective Inhibition of Alzheimer Disease-Like Tau Aggregation by Phenothiazines *Proceedings of the National Academy of Sciences* **1996**, *93*, 11213-11218.
- [54] Brunden, K.R.; Trojanowski, J.Q.; Lee, V.M.Y. Advances in Tau-Focused Drug Discovery for Alzheimer's Disease and Related Tauopathies *Nature reviews Drug discovery* **2009**, *8*, 783-793.

-
- [55] Biju, K.C.; Evans, R.C.; Shrestha, K.; Carlisle, D.C.; Gelfond, J.; Clark, R.A. Methylene Blue Ameliorates Olfactory Dysfunction and Motor Deficits in a Chronic MPTP/Probenecid Mouse Model of Parkinson's Disease *Neuroscience* **2018**, *380*, 111-122.
- [56] Kim, J.; Cote, L.J.; Kim, F.; Yuan, W.; Shull, K.R.; Huang, J. Graphene Oxide Sheets at Interfaces *Journal of the American Chemical Society* **2010**, *132*, 8180-8186.
- [57] Lucchese, M.M.; Stavale, F.; Ferreira, E.M.; Vilani, C.; Moutinho, M.V.O.; Capaz, R.B. Quantifying Ion-Induced Defects and Raman Relaxation Length in Graphene *Carbon* **2010**, *48*, 1592-1597.
- [58] Gonçalves, G.; Vila, M.; Bdikin, I.; De Andrés, A.; Emami, N.; Ferreira, R.A.; Carlos, L.D.; Grácio, J.; Marques, P.A. Breakdown Into Nanoscale of Graphene Oxide: Confined Hot Spot Atomic Reduction and Fragmentation *Scientific reports* **2014**, *4*, 6735.
- [59] Chong, Y.; Ge, C.; Yang, Z.; Garate, J.A.; Gu, Z.; Weber, J.K.; Zhou, R. Reduced Cytotoxicity of Graphene Nanosheets Mediated by Blood-Protein Coating *ACS nano* **2015**, *9*, 5713-5724.
- [60] Duan, G.; Kang, S.G.; Tian, X.; Garate, J.A.; Zhao, L.; Ge, C.; Zhou, R. Protein Corona Mitigates the Cytotoxicity of Graphene Oxide by Reducing its Physical Interaction with Cell Membrane *Nanoscale* **2015**, *7*, 15214-15224.
- [61] Vranic, S.; Rodrigues, A.F.; Buggio, M.; Newman, L.; White, M.R.H.; Spiller, D.G.; Bussy, C.; Kostarelos K. Live Imaging of Label-Free Graphene Oxide Reveals Critical Factors Causing Oxidative-Stress-Mediated Cellular Responses *ACS Nano* **2018**, *12*, 1373-1389.
- [62] Reina, G.; Ruiz, A.; Murera, D.; Nishina, Y.; Bianco A. "Ultramixing": A Simple and Effective Method To Obtain Controlled and Stable Dispersions of Graphene Oxide in Cell Culture Media *ACS Appl. Mater. Interfaces* **2019**, *11*, 7695- 7702.
- [63] Simsikova, M.; Sikola, T. Interaction of Graphene Oxide With Proteins and Applications of Their Conjugates *J Nanomed Res* **2017**, *5*, 00109
- [64] Zhang, L.; Xia, J.; Zhao, Q.; Liu, L.; Zhang, Z. Functional Graphene Oxide As a Nanocarrier for Controlled Loading and Targeted Delivery of Mixed Anticancer drugs *Small* **2010**, *6*, 537-544.
- [65] Wu, C.; Wang, L.; Harbottle, D.; Masliyah, J.; Xu, Z. Studying Bubble-Particle Interactions by Zeta Potential Distribution Analysis *Journal of colloid and interface science* **2015**, *449*, 399-408.
- [66] Casals, E.; Pfaller, T.; Duschl, A.; Oostingh, G.J.; Puntès, V. Time Evolution of the Nanoparticle Protein Corona *ACS Nano*, **2010**, *4*, 3623-3632.
- [67] Yang, L.; Zhang, R.; Liu, B.; Wang, J.; Wang, S.; Han, M.Y.; Zhang, Z. Π -Conjugated Carbon Radicals at Graphene Oxide to Initiate Ultrastrong Chemiluminescence *Angewandte Chemie International Edition* **2014**, *53*, 10109-10113.

-
- [68] Belyanskaya, L.; Manser, P.; Spohn, P.; Bruinink, A.; Wick, P. The Reliability and Limits of the MTT Reduction Assay for Carbon Nanotubes–Cell Interaction *Carbon* **2007**, *45*, 2643-2648.
- [69] Gies, V.; Zou, S. Systematic Toxicity Investigation of Graphene Oxide: Evaluation of Assay Selection, Cell Type, Exposure Period and Flake Size *Toxicol. Res.* **2018**, *7*, 93-101.
- [70] Alber, F.; Dokudovskaya, S.; Veenhoff, L.M.; Zhang, W.; Kipper, J.; Devos, D.; Suprpto, A.; Karni-Schmidt, O.; Williams, R.; Chait, B.T.; Sali, A. The Molecular Architecture of the Nuclear Pore Complex *Nature* **2007**, *450*, 695-701.
- [71] Jaworski, S.; Sawosz, E.; Grodzik, M.; Winnicka, A.; Prasek, M.; Wierzbicki, M.; Chwalibog, A. In Vitro Evaluation of the Effects of Graphene Platelets on Glioblastoma Multiforme Cells *International journal of nanomedicine* **2013**, *8*, 413-420.
- [72] Oh, J.Y.; Kim, H.S.; Palanikumar, L.; Go, E.M.; Jana, B.; Park, S.A.; Kim, H.Y.; Kim, K.; Seo, J.K.; Kwak, S.K.; Kim, C.; Kang, S.; Ryu J.-H. Cloaking Nanoparticles with Protein Corona Shield for Targeted Drug Delivery. *Nature Communications* **2018**, *9*, 4548.
- [73] Calabuig, A.; Mugnano, M.; Miccio, L.; Grilli, S.; Ferraro, P. Investigating Fibroblast Cells Under “Safe” and “Injurious” Blue-Light Exposure by Holographic Microscopy *Journal of biophotonics* **2017**, *10*, 919-927.
- [74] Paturzo, M.; Pagliarulo, V.; Bianco, V.; Memmolo, P.; Miccio, L.; Merola, F.; Ferraro, P. Digital Holography, a Metrological Tool for Quantitative Analysis: Trends and Future Applications *Optics and Lasers in Engineering* **2017**, *104*, 32-47.
- [75] Fusco, S.; Memmolo, P.; Miccio, L.; Merola, F.; Mugnano, M.; Paciello, A.; Ferraro P.; Netti, P.A. Nanomechanics of a Fibroblast Suspended Using Point-Like Anchors Reveal Cytoskeleton Formation *RSC Adv.* **2016**, *6*, 24245-24249.
- [76] Wang, X.; Chen, Y.P.; Nolte, D.D. Strong Anomalous Optical Dispersion of Graphene: Complex Refractive Index Measured by Picometry *Opt. Express* **2008**, *16*, 22105-22112.
- [77] Krishnamoorthy, K.; Veerapandian, M.; Yun, K.; Kim, S.J. The Chemical and Structural Analysis of Graphene Oxide with Different Degrees of Oxidation *Carbon* **2013**, *53*, 38-49.